

Use of synchrotron-based radiography to diagnose pulsed power driven wire explosion experiments

Cite as: Rev. Sci. Instrum. 90, 013504 (2019); doi: 10.1063/1.5055949
Submitted: 12 September 2018 • Accepted: 18 December 2018 •
Published Online: 11 January 2019



S. P. Theocharous,^{1,a)} S. N. Bland,¹  D. Yanuka,¹ A. Rososhek,²  M. P. Olbinado,³ A. Rack,³ 
and Ya. E. Krasik² 

AFFILIATIONS

¹ Plasma Physics Group, Imperial College London, London SW7 2BW, United Kingdom

² Physics Department, Technion—Israel Institute of Technology, Haifa 32000, Israel

³ European Synchrotron Radiation Facility, CS 40220, 38043 Grenoble Cedex 9, France

^{a)} Electronic mail: savva.theocharous12@imperial.ac.uk

ABSTRACT

We describe the first use of synchrotron radiation to probe pulsed power driven high energy density physics experiments. Multi-frame x-ray radiography with interframe spacing of 704 ns and temporal resolution of <100 ps was used to diagnose the electrical explosion of different wire configurations in water including single copper and tungsten wires, parallel copper wire pairs, and copper x-pinch. Such experiments are of great interest to a variety of areas including equation of state studies and high pressure materials research, but the optical diagnostics that are usually employed in these experiments are unable to probe the areas behind the shock wave generated in the water, as well as the internal structure of the exploding material. The x-ray radiography presented here, performed at beamline ID19 at European Synchrotron Radiation Facility (ESRF), was able to image both sides of the shock to a resolution of up to 8 μm , and phase contrast imaging allowed fine details of the wire structure during the current driven explosion and the shock waves to be clearly observed. These results demonstrate the feasibility of pulsed power operated in conjunction with synchrotron facilities, as well as an effective technique in the study of shock waves and wire explosion dynamics.

Published under license by AIP Publishing. <https://doi.org/10.1063/1.5055949>

I. INTRODUCTION

Pulsed power is often used to drive high energy density physics (HEDP) experiments, exploring topics including laboratory astrophysics,^{1,2} high pressure materials,³ and inertial confinement fusion experiments.^{4,5} Perhaps the simplest experiment of this kind involves the explosion of a single thin metal wire either in a vacuum or in a medium such as water.⁶ Such experiments are often used to perform equation of state studies, and more recently, the shock waves generated in water by exploding wires have become of interest for efficiently producing high pressure conditions at the meeting point of multiple shock waves generated by arrays of wires in a cylindrical or spherical geometry.^{7,8} Wire explosions in water, rather than gas or vacuum, are often preferred as high breakdown voltage prevents the formation of plasma on the

wire's surface, and as the low compressibility of water slows the expansion of the wire and ensures high energy density deposition in the wire material.

Most previous experiments with wires in water have used optical probing techniques in conjunction with electrical diagnostics to measure energy input to the wires. However, these diagnostics have been unable to probe behind the shocks,⁹ probably due to unwanted and incalculable refraction of the light by turbulence in this region. As a result, these diagnostics can locate the position of the shock wave by the point where the transmission drops significantly, but cannot probe behind the shock wave to measure density, or observe the structure of the wire material that remains to investigate the dynamics of the explosion. The greater transmission of x-rays through these materials could solve this problem, but the past attempts

at x-ray radiography of underwater exploding wires employed a relatively large-scale vacuum x-ray diode source, which produced relatively noisy and low-resolution images that could not resolve the shock waves or the exploding wire internal structure.¹⁰ Proton radiography has also been attempted to image underwater wire explosions; however, these experiments suffered from a significant shot-to-shot variation in the beam and poor spatial resolution.¹¹

In contrast to these cases, synchrotron sources can provide multiple high intensity pulses of near-parallel x-ray flux that are closely spaced in time, allowing imagery of multiple frames per experiment to be taken to fully track the time evolution of a system. Additionally, when the source has a sufficiently high degree of partial spatial coherence, as can be the case on synchrotron systems with sufficient propagation length between the x-ray source and the target to be imaged, propagation based Phase Contrast Imaging (PCI) can be achieved.^{12,13} In this regime, interference of diffracted x-rays causes an increase in contrast on the boundaries with sharp changes in refractive index, resulting in the enhancement in appearance of shock boundaries or the boundaries between different materials. Recently, shock wave propagation in water has been imaged using similar techniques at European Synchrotron Radiation Facility (ESRF) in experiments in which the shocks were laser induced.¹⁴

In this paper, we present the details of the wire explosion experiments we conducted using pulsed power coupled to a synchrotron—in this case, ID19 at ESRF. This was used to diagnose single wire, two wire, and x-pinch wire explosions. Although only radiography measurements of shocks are presented here, the experiments demonstrate the potential for the use of pulsed power apparatus in conjunction with synchrotron facilities, which could be used concurrently to support any x-ray based diagnostic techniques, including diffraction and absorption spectrum techniques,¹⁵ and is not limited to shock experiments.

II. ID19 BEAMLINE AND X-RAY IMAGING

In order to image the wire material and shocks produced in the water by the wire explosions, a uniform x-ray beam of diameter ~ 10 mm was required, with the additional condition of high partial spatial coherence for PCI. The experiments also required a sufficiently intense beam with suitably high energy photons to transmit through the ~ 20 mm of water in which the wire explosions were conducted, and a pulse length that provided enough photons for each frame without being so long as to compromise temporal resolution.

The experiments described were conducted at the ID19 beamline at ESRF. This beamline is typically used for 3D imaging such as microtomography, but the small source size and large undulator source-to-target distance (~ 150 m) allows for a beam with a high degree of partial spatial coherence such that phase contrast imagery is possible.¹⁶

The synchrotron operates a number of ring filling modes. The commonly used modes, along with the corresponding

numbers of photons per pulse generated at ID19, have been summarised by Olbinado *et al.*¹⁴ The modes that generate more frequent x-ray pulses utilise a fewer electrons per bunch in the ring and thus produce lower intensity x-ray pulses, resulting in a compromise between x-ray pulse frequency and intensity. In these experiments, 4-bunch mode was utilised, with x-ray pulses occurring with a time interval between bunches of 704 ns. This was an adequate match to the timescales of our experiments, which were similar to previous wire explosion experiments using generators with rise times of approximately a microsecond.¹⁷ The duration of each pulse, and thus the effective exposure of each radiograph image, is given by the bunch duration, which is 55 ps in 4-bunch mode. We have since performed additional experiments in the 16-bunch mode, with images captured every third pulse (due to the limits in camera speed) resulting in an interframe time of 528 ns.

ID19's two U32 undulators were operated at minimum gap of 11.1 mm and 11.5 mm in order to maximise the spectral flux, giving an x-ray energy spectrum of ~ 20 keV– ~ 50 keV, with mean energy of ~ 30 keV. Complete predictions of the spectral flux with these undulator settings were performed by Escuiza *et al.*¹⁸ To minimise heating of the target, particularly the water, and the scintillator, a 1.4 mm diamond filter and a 0.7 mm aluminium filter were positioned in the beam path. The total duration of exposure of the system to the x-ray pulses was limited using a fast shutter to 0.2 s.

ID19 had 2 separate “hutches” on the x-ray beam path in which experiments can be conducted. The experiments discussed here were conducted in the hutch closer to the source, through which the x-rays travel before reaching the rear hutch, in which our camera and scintillator were located. This allowed a larger experiment-to-camera distance, enhancing the appearance of boundaries using PCI, and this hutch had a convenient space where the experiment could be mounted.

We used an indirect imaging setup, optimised for MHz frame rate imaging, as reported by Olbinado *et al.*¹⁴ The optical camera used was a Hyper Vision HPV-X2 (Shimadzu Corp., Japan), which has a $30 \mu\text{m} \times 21.3 \mu\text{m}$ CMOS sensor, capable of imaging 400×250 pixel images at up to 5×10^6 fps, storing 128 images in one recording sequence. As the rate of x-ray pulses were at lower frequency than this, the frame rate of the system was limited by the frequency of the x-ray pulses from the synchrotron. The camera exposure time was 400 ns. The bit depth of the camera is 10-bits, with dark noise of approximately 7 counts. The radiographs were converted to a detectable frequency using a commercially available $250 \mu\text{m}$ thick LYSO:Ce scintillator crystal, chosen for its short decay time (≈ 40 ns), negligible afterglow, and reasonable emission overlap with the HPV-X2 camera spectral response.¹⁴ A 45° mirror was used to prevent direct exposure of the camera to x-rays. The use of this indirect x-ray detection system allowed alterations of magnifications using only conventional optics; in these experiments, measurements were taken with two lens systems. A $1\times$ low-magnification setup with a

resolution of $32\ \mu\text{m}$ per pixel corresponding to a field-of-view of $12.8\ \text{mm} \times 8\ \text{mm}$ was used to observe shock waves over long distances and large scale instabilities/interactions of neighbouring wires. A $4\times$ high-magnification setup with a resolution of $8\ \mu\text{m}$ per pixel corresponding to a field-of-view of $3.2\ \text{mm} \times 2\ \text{mm}$ showed the details of the launch of shock waves and the finer scale instabilities that were discovered in the wires as they exploded. Both of these systems had a numerical aperture of 0.2.

The interference fringes for PCI occur in the Fresnel diffraction regime. The spacing of adjacent maxima generated in this regime by a step-like target like a discrete edge, given by $1.7\sqrt{\lambda D}$ where λ is the photon wavelength and D is the target-to-detector distance, gives a reasonable estimate of the required distance to achieve PCI.¹² Thus, a sample-to-detector distance of 10 m was used for the $1\times$ low magnification configuration, compared with a distance of 5 m for the $4\times$ configuration. Using the wavelength of the mean x-ray frequency ($4.1 \times 10^{-11}\ \text{m}$), this distance between maxima is $34\ \mu\text{m}$ for the low-magnification setup and $24\ \mu\text{m}$ for the high-magnification setup, with the corresponding camera resolutions for the two configurations able to resolve the resultant fringes. The mean x-ray frequency is used here to give an approximate spatial scale for the resulting diffraction pattern. However, in these experiments, the broadband characteristic of the x-ray beam results in the superposition of many single-frequency PCI patterns. Despite this, the peak of x-ray deviation occurs at the refractive index boundary independent of wavelength, and thus, the initial redistribution fringe provides contrast even with broadband sources,¹³ although higher order fringes are likely to be blurred.

The transmission of 30 keV x-rays through $200\ \mu\text{m}$ copper is approximately 15%, and transmission of 10 mm of water is approximately 72%.¹⁹ Hence, x-rays of this energy should lead to good contrast between the wires and water in the resulting radiograph. Using hydrodynamic simulations as described by Yanuka *et al.*,²⁰ the water density behind the shock is $\sim 10\%$ greater than in front, resulting in a difference in transmission across the shock of $\sim 3\%$. This is an upper bound on the radiograph contrast, which is significantly reduced by the $<10\ \text{mm}$ shock diameter from the majority of the experiment, and the decrease in x-ray path through the denser water closer to the shock, as the explosion is cylindrical. As this transmission difference is small, phase contrast is required to image the density difference corresponding to the shock. The ability to image these small transmission differences was explored in background imaging tests where small bubbles on the inside surface of a cylinder were imaged. Despite only small differences in transmission as a result of these bubbles, the outlines of the bubbles were readily observable in the radiographs as a result of phase contrast effects.

Ten two-dimensional compound refractive lenses are used to collimate the x-ray beam. This leads to some beam non-uniformity that is visible in results, with a notable

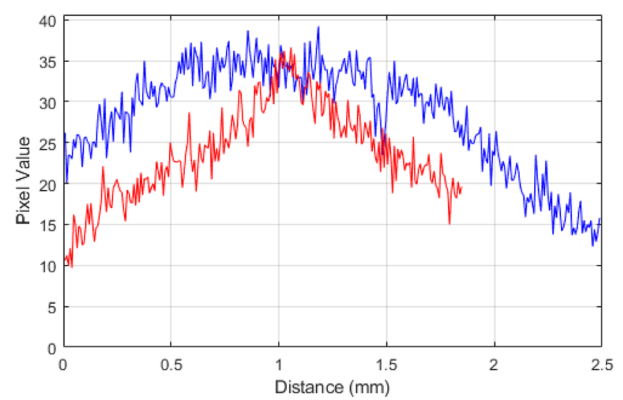
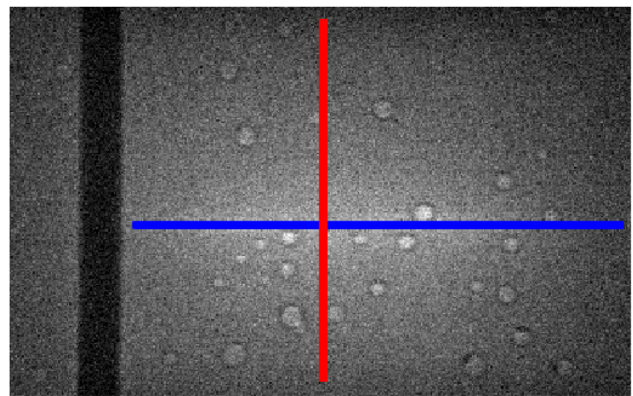


FIG. 1. Example pre-explosion image of the high-magnification configuration, with perpendicular lineouts demonstrating the non-uniform intensity profile. Horizontal lineout is left to right, and vertical is top to bottom. The lineouts are averaged over the width of the lines on the radiograph (5 pixels).

“hotspot” in the centre of the image, as shown in Fig. 1. This shows a single high-magnification radiograph pre-wire explosion in which the wire was placed off-centre. Two lineouts are plotted to show the non-uniformity vertically and horizontally. It should be noted that this image has not been processed for noise or corrected for the different path lengths through water that the x-rays for corresponding pixels take; however, as the container is cylindrical, the greatest path length through water is in the centre of the image, this correction would only increase the brightness difference between the centre and edge of the image in the horizontal lineout.

III. PULSED POWER SETUP

The pulsed power for the experiments was provided by a compact pulser system that was designed and manufactured at Technion. The pulser was controlled from outside of the hutch by the control panel whilst the rest of the components of the pulser were within the hutch, local to the load. The control panel controlled the charging of the capacitors in the pulser and safety interlock that could be connected

to the hutch door. The pulser contained four 50 kV Maxwell pulse capacitors, each with capacitance of 220 nF, which were charged to 32 kV (corresponding to a total stored energy of approximately 450 J) immediately before the experiment. The pulser had a rise time of approximately 1000 ns. Discharge current was measured using a 0.027 Ω current viewing resistor, and voltage was measured using a voltage divider on the high-voltage electrode.

Experiments were conducted with 3 principal wire configurations. These were as follows:

1. Single wire configuration, in which all of the current passes through one vertical wire.
2. Two wire configuration, in which the current is divided between 2 vertical wires, suspended parallel with a distance of approximately 2.5 mm between them.
3. X-pinch configuration, in which the 2 wires were each suspended in the same plane at approximately 40° such that they made contact with each other at the crossing point.

The wires used were copper or tungsten, between 130 μm and 200 μm thickness and approximately 45 mm in length. These parameters were chosen to maximise the energy deposition into the wires, therefore critically damping the current oscillation, preventing current ringing. The x-ray beam propagation was perpendicular to the wires in all cases.

The experimental load was held in an aluminium experimental chamber, with 10 mm circular windows on either side to allow the x-ray beam to enter and exit, covered by thin mylar sheets. Inside the chamber, the wires were held in a water-filled cylindrical acrylic tube that was destroyed during each shot. These cylinders had 8 mm inner diameter and 1.5 mm thickness for the single wire configuration, and 17 mm inner diameter and 3 mm thickness for the two configurations with two wires. A diagram of the chamber is shown in Fig. 2.

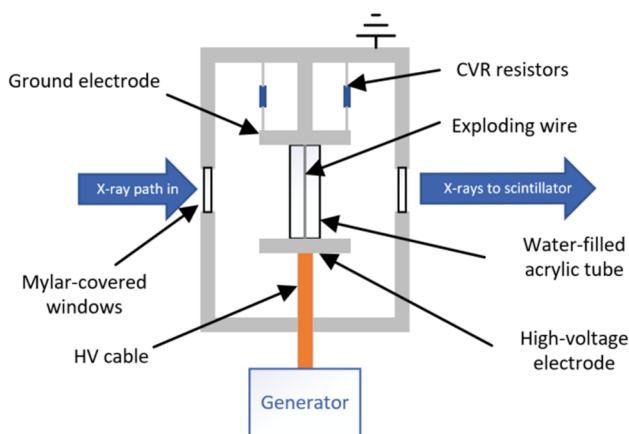


FIG. 2. Cross section diagram of experimental chamber.

Several key factors were considered in the design of the generator to make it suitable for experiments on a synchrotron:

- Jitter: many pulsed power systems have unacceptably high jitter (on the order of 100 ns) due to low trigger voltages or high inductance switch design. This would lead to unpredictable timings of the resultant images from each experiment. The generator used here featured a low profile “pancake” spark gap that was used to connect the capacitors to the load. This spark gap was triggered by a PT-55 like spiral generator,²¹ capable of producing a 50 kV pulse with a rise time of approximately 5 ns. The overall jitter of the system, from the initial trigger pulse to start of output current, was less than ± 10 ns.
- Electromagnetic noise: pulsed power systems often generate a significant electromagnetic noise when firing. All of the components were fully enclosed, and all enclosures grounded, with any connections made using a well-shielded coaxial cable, to reduce any electromagnetic noise issues that could have otherwise affected electronics in the hutch.
- Repeatability: The wires were soldered into a cartridge that was screwed into place in the chamber, which remained fixed throughout the experiment. This ensured that the wires were always positioned similarly and that the system did not have to be realigned between shots. This also made the system fast to reload, which is especially important when beamtime is limited.
- Debris mitigation: The generated shock waves could potentially break apparatus. The chamber was therefore mounted separately from any other apparatus, and the acrylic cylinder was designed to break safely and was contained in the fully enclosed experimental chamber.

Prior to the experiments, the system was rigorously tested in the offline experiments including European Economic Area CE certification of the control panel to Low Voltage Directive (LVD) and Electromagnetic Compatibility (EMC) standards, and tests of the high voltage and safety systems were repeated after reassembly at ESRF.

IV. TIMING AND SYNCHRONISATION

It was important that the pulsed power fired with repeatable timing relative to the x-rays, but also that it could be manually triggered by the user. The timing scheme used here is a modification of the system used by Olbinado *et al.*²² A clock signal that was synchronised with the x-ray pulses was generated by the ESRF in-house developed bunch clock delay unit. This clock signal was input into a digital input/output module that could be manually triggered using the beamline computer. On triggering, this system produced a transistor-transistor logic (TTL) signal that was at a fixed point in the x-ray pulse cycle, ensuring synchronisation. This trigger signal was input to a low jitter delay box (DG645; Stanford Research

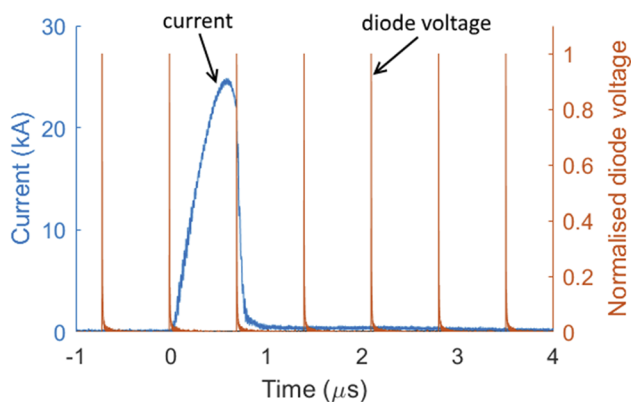


FIG. 3. Graph showing the response of the x-ray diode (i.e., timing of the x-ray pulses) and the measured current in the pulser for a single experiment, after correction for cable delays and offset on the x-axis such that the foot of the current pulse is at $t = 0$.

Systems, USA), which controlled both the pulser and an oscilloscope that was recording pulse current and voltage diagnostics. The timing of the trigger pulse to the pulser was then varied to fully view the time evolution of the system or isolate a specific stage of the wire explosion process. Timings were then adjusted for start of current and cable propagation delay in post-processing to obtain absolute timing of frames relative to the start of the current pulse.

The HPV-X2 camera was triggered by a second delay box, which itself was triggered simultaneously to the first. This started the recording of a series of frames at fixed frame rate. The frame rate used was 700 ns, as it was only possible to adjust this frame rate in increments of 10 ns. As the experiments were $<5 \mu\text{s}$ in duration, this was sufficiently close to the x-ray pulse frequency with the camera integration time used to image the experiments fully.

It was not possible to view the relative timing of the x-ray pulses during the experiment, as the beam was too narrow to include an x-ray detector at any point in the beam without obscuring the radiograph images. Instead, the timing of the x-ray pulses was measured on separate tests with identical triggering setup to the explosion experiments, but without firing the pulser. For these tests, a fast Si x-ray photodiode (G4176-03; Hamamatsu Photonics K.K., Japan) was placed directly in front of the window of the experimental chamber. The signal was recorded using a high-voltage bias tee (Model 5531; Picosecond Pulse Labs, USA). From this, it was possible to record the timing of the x-ray pulses relative to the trigger signal from the bunch clock delay unit. This measurement was repeated 3 times over the ~ 36 h over which these measurements were conducted to correct for any drift. However, this was found to be very stable, with differences in timing on a sub-nanosecond scale between these measurements.

Figure 3 shows a graph of the timing used for an example experiment. The current measured using a current viewing resistor is plotted with x-ray diode response from a test with equivalent timings, with both signals corrected for cable length signal propagation delay. Each x-ray pulse corresponds to a single frame output from the camera. The X-axis is shifted such that $x = 0$ is at the foot of the current pulse so that the timing of the x-ray pulses corresponds to the absolute timing in the experiment of each frame, giving accurate timings for each frame in each radiograph series. This allowed for accurate timing when combining results from repeats with different delays.

V. RESULTS

Figure 4 shows a series of radiographs obtained from a single experiment in the low magnification configuration, using a single $200 \mu\text{m}$ copper wire. The frames displayed are consecutive, with 704 ns spacing. The dark circle around the edge corresponds to the edge of the window of the

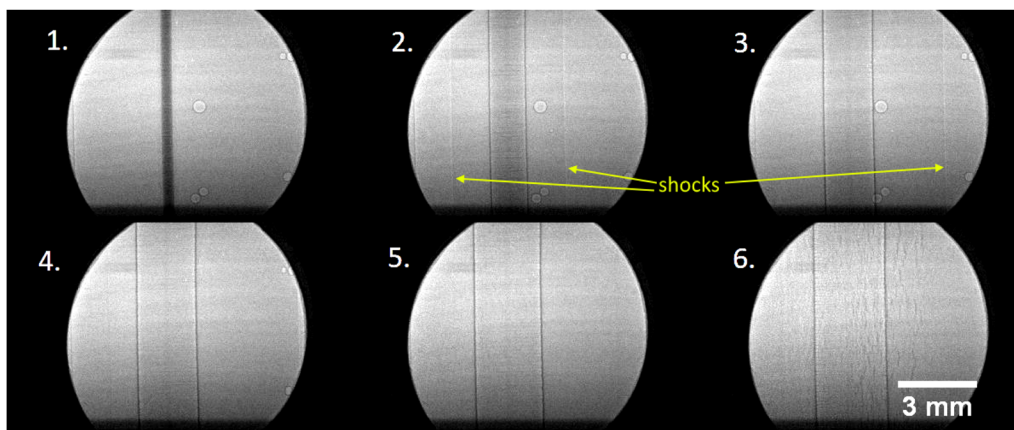


FIG. 4. Consecutive X-ray radiographs of a single $200 \mu\text{m}$ copper wire explosion in the low magnification configuration. Time delay between frames is 704 ns.

chamber (although it is not fully circular as the chamber is slightly rotated off axis). Frame 1 shows the wire early in the experiment, before current through the wire.

Frame 2 shows the start of expansion of the wire. The expansion of the wire material has launched a cylindrical shock wave into the surrounding water. The sections of the boundary between the rapidly expanding copper and water and the density change across the shock front that are parallel to the x-rays are both enhanced by PCI, allowing distance from the source and thus average speed between frames to be measured. Both of these boundaries remain visible in frame 3, and on the right hand side of the image, the shock remains visible in frame 4. Measurements of the positions of this shock show that it is traveling at approximately 2000 m/s. This means that the distance traveled by this shock over the length of a single x-ray pulse is $<2 \mu\text{m}$, which is less than our maximum spatial resolution and demonstrates that our temporal resolution is sufficient to capture the position of the shocks accurately.

In some experiments, air bubbles were purposefully left attached to the inner edge of the acrylic cylinder, as a measure of the arrival time of the shock wave at the cylinder. Air bubbles of approximately 0.1 mm–0.5 mm attached to the inner edge of the acrylic cylinder are visible in the earlier frames. The central bubbles appear to collapse between frames 3 and 4, with the bubbles on the far edge collapsing between frames

4 and 5. This indicates that the wire is not perfectly central in the cylinder, as is visible in the image, as it is likely that these are collapsed by the shock wave, which should expand uniformly cylindrically from the wire.

In the final frame, small vertical fractures can be seen across the image. These are cracks in the acrylic and appear to be the early stage of the shattering of the acrylic tube as a result of the shock. Later frames show this cylinder shattering entirely. This may limit the potential to view late stage processes in the experiment (e.g., instability evolution in the metal-water boundary or shock reflection off the wall of the container), and attempts to minimise this effect in future (e.g., larger diameter cylinder) could compromise total x-ray transmission, resulting in noisier images. Alternatively, this effect could be used the basis of an experiment testing the material properties of similar cylinders.²³

Figure 5 shows example pre- and post-explosion high magnification images for the x-pinch configuration. In this

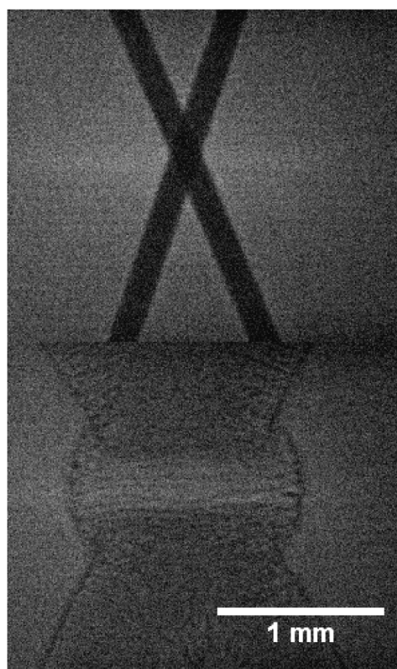


FIG. 5. X-ray radiographs of pre- and post-explosion of an x-pinch made using $160 \mu\text{m}$ copper wires in the high magnification configuration. The delay between the two images is 1408 ns (2 frames), with explosion beginning within the first 704 ns.

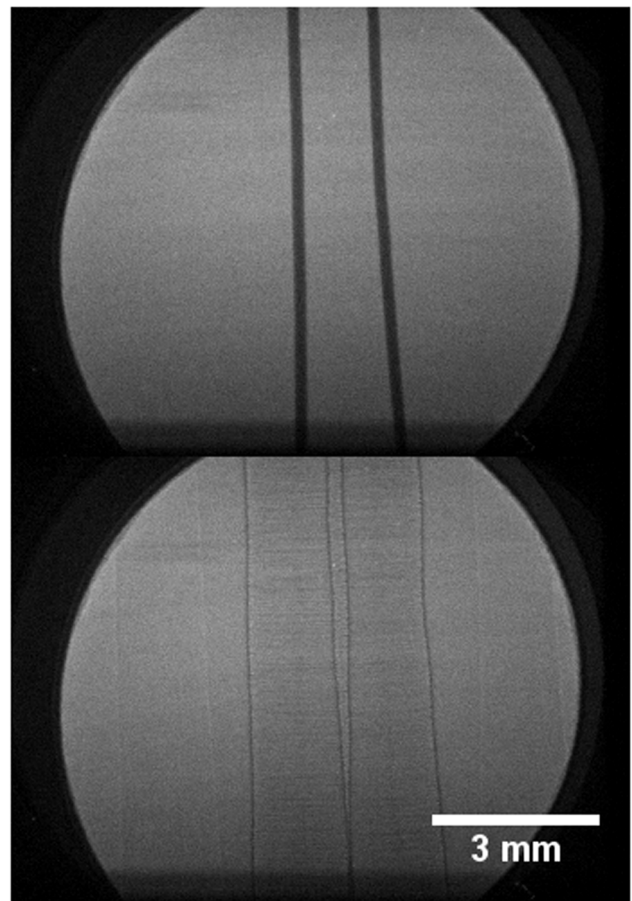


FIG. 6. X-ray radiographs of pre- and post-explosion of two parallel $160 \mu\text{m}$ copper wires in the low magnification configuration. The delay between the two images is 2112 ns (3 frames), with explosion beginning within the first 704 ns.

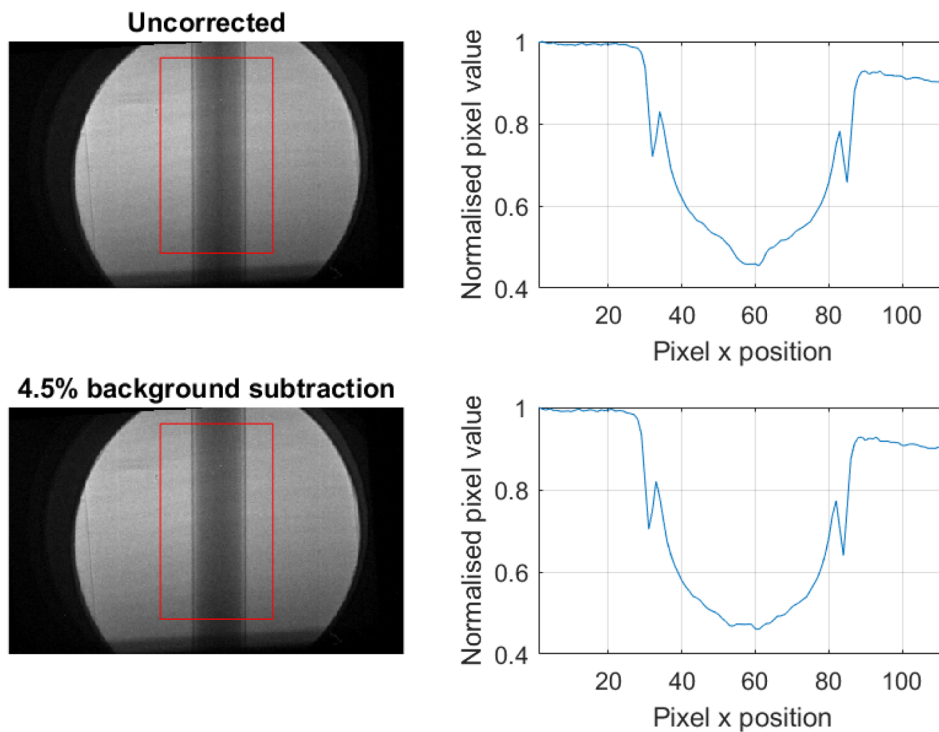


FIG. 7. Radiographs of an uncorrected (top), and corrected with 4.5% background subtraction (bottom), frame from a single tungsten wire explosion, and the corresponding y-averaged lineouts. The lineouts correspond to the averages of each pixel vertical column within the red boxes. An area of lower than expected intensity is visible in the uncorrected lineout at around $x = 55$ – $x = 62$, corresponding to the initial position of the wire in the background images. This is not visible in the lower corrected radiograph. The background used for subtraction was the mean of the eight pre-explosion frames that were recorded.

image, the shocks from each of the two wires are visible, as well as an interaction region between the two wires. Likewise, Fig. 6 shows example pre- and post-explosion low magnification images for the two wire configuration. The copper-water interface is clearly visible in the exploded image, along with some instability.

We observed that the radiographs often displayed an area of lower intensity at the position of the pre-exploded wire in the immediately post-explosion frames. Despite the ostensibly fast decay of the scintillator, it is likely that this is an artefact due to the overexposure of the area around the wire pre-explosion, as it is exposed to multiple x-ray pulses before explosions occurs, resulting in a persistence of the background image. Rutherford *et al.*²⁴ indicate that, using calculations based on decay parameters from literature, an equivalent LYSO:Ce scintillator should observe a negligible background on each frame at ID19 on 4-bunch mode. However, subtraction of varying levels of background and observation of lineouts across the image indicate backgrounds of up to 5% of frames immediately after explosions. This is highlighted in Fig. 7, which shows a comparison between lineouts across an uncorrected post-explosion frame, and a frame with 4.5% background subtraction.

This indicates that this is not an effect resulting from conventional decay and may arise as a result of other effects, such as temperature dependence and small amounts of contaminants in the crystal, or as a result of insufficient data about the higher order decay parameters of these crystals. However, it is difficult to quantify this effect any further here as the

dynamics of the explosions dominate changes of intensity between frames.

A full analysis of the results obtained, with the analysis of the processes observed, will be published in the future reports.

VI. SUMMARY

We have conducted the first pulsed power experiments conducted on a synchrotron facility. Single, parallel and x-pinch configuration wires were exploded in water and x-rays from ESRF at ID19 were used to perform radiography and PCI to image the system at 1.4 MHz, with spatial resolution of $8\ \mu\text{m}$ and temporal resolution of $<100\ \text{ps}$. More generally, the work demonstrates the compatibility of pulsed power technology with synchrotron facilities.

ACKNOWLEDGMENTS

This research was funded by EPSRC, First Light Fusion Ltd, The Institute of Shock Physics, Sandia National Laboratories, and U.S. Department of Energy under Cooperative Agreement Nos. DE-NA0003764 and DE-SC0018088. Beamtime was kindly granted for experiment HC/3419 BLAND ID19 30-04-2018/02-05-2018 by ESRF.

The authors would also like to thank Harald Reichert of ESRF, Paul Berkvens and the safety team at ESRF, W. G. Proud and D. Chapman of Imperial College, D. Eakins of Oxford University, and F. Zucchini and C. Chauvin of CEA Gramat

for their support in planning these experiments, and S. Gleizer and E. Flyat of Technion for their generous technical support.

REFERENCES

- ¹J. D. Hare, L. G. Suttle, S. V. Lebedev, N. F. Loureiro, A. Ciardi, J. P. Chittenden, T. Clayson, S. J. Eardley, C. Garcia, J. W. D. Halliday, T. Robinson, R. A. Smith, N. Stuart, F. Suzuki-Vidal, and E. R. Tubman, *Phys. Plasmas* **25**, 055703 (2018).
- ²F. Suzuki-Vidal, S. Lebedev, M. Krishnan, J. Skidmore, G. Swadling, M. Bocchi, A. Harvey-Thompson, S. Patankar, G. Burdiak, P. de Grouchy, L. Pickworth, S. Stafford, L. Suttle, M. Bennett, S. Bland, J. Chittenden, G. Hall, E. Khoory, R. Smith, and P. Coleman, *High Energy Density Phys.* **9**, 141 (2013).
- ³X. Zhang, G. Wang, J. Zhao, F. Tan, B. Luo, and C. Sun, *Rev. Sci. Instrum.* **85**, 055110 (2014).
- ⁴R. Leeper, T. Alberts, J. Asay, P. Baca, K. Baker, S. Breeze, G. Chandler, D. Cook, G. Cooper, C. Deeney, M. Derzon, M. Douglas, D. Fehl, T. Gilliland, D. Hebron, M. Hurst, D. Jobe, J. Kellogg, J. Lash, and D. Peterson, *Nucl. Fusion* **39**, 1283 (2002).
- ⁵M. R. Gomez, S. A. Slutz, A. B. Sefkow, D. B. Sinars, K. D. Hahn, S. B. Hansen, E. C. Harding, P. F. Knapp, P. F. Schmit, C. A. Jennings, T. J. Awe, M. Geissel, D. C. Rovang, G. A. Chandler, G. W. Cooper, M. E. Cuneo, A. J. Harvey-Thompson, M. C. Herrmann, M. H. Hess, O. Johns, D. C. Lamppa, M. R. Martin, R. D. McBride, K. J. Peterson, J. L. Porter, G. K. Robertson, G. A. Rochau, C. L. Ruiz, M. E. Savage, I. C. Smith, W. A. Stygar, and R. A. Vesey, *Phys. Rev. Lett.* **113**, 155003 (2014).
- ⁶Y. Krasik, A. Grinenko, A. Sayapin, S. Efimov, A. Fedotov, V. Gurovich, and V. Oreshkin, *IEEE Trans. Plasma Sci.* **36**, 423 (2008).
- ⁷S. N. Bland, Y. E. Krasik, D. Yanuka, R. Gardner, J. MacDonald, A. Virozub, S. Efimov, S. Gleizer, and N. Chaturvedi, *Phys. Plasmas* **24**, 082702 (2017).
- ⁸A. Rososhek, S. Efimov, M. Nitishinski, D. Yanuka, S. V. Tewari, V. T. Gurovich, K. Khishchenko, and Y. E. Krasik, *Phys. Plasmas* **24**, 122705 (2017).
- ⁹Y. E. Krasik, S. Efimov, D. Sheftman, A. Fedotov-Gefen, O. Antonov, D. Shafer, D. Yanuka, M. Nitishinskiy, M. Kozlov, L. Gilburd, G. Toker, S. Gleizer, E. Zvulun, V. T. Gurovich, D. Varentsov, and M. Rodionova, *IEEE Trans. Plasma Sci.* **44**, 412 (2016).
- ¹⁰D. Sheftman, D. Shafer, S. Efimov, K. Gruzinsky, S. Gleizer, and Y. E. Krasik, *Rev. Sci. Instrum.* **83**, 103505 (2012).
- ¹¹D. Varentsov, O. Antonov, A. Bakhmutova, C. W. Barnes, A. Bogdanov, C. R. Danly, S. Efimov, M. Endres, A. Fertman, A. A. Golubev, D. H. H. Hoffmann, B. Ionita, A. Kantsyrev, Y. E. Krasik, P. M. Lang, I. Lomonosov, F. G. Mariam, N. Markov, F. E. Merrill, V. B. Mintsev, D. Nikolaev, V. Panyushkin, M. Rodionova, M. Schanz, K. Schoenberg, A. Semennikov, L. Shestov, V. S. Skachkov, V. Turtikov, S. Udrea, O. Vasylyev, K. Weyrich, C. Wilde, and A. Zubareva, *Rev. Sci. Instrum.* **87**, 023303 (2016).
- ¹²P. Cloetens, R. Barrett, J. Baruchel, J.-P. Guigay, and M. Schlenker, *J. Phys. D: Appl. Phys.* **29**, 133 (1996).
- ¹³S. W. Wilkins, T. E. Gureyev, D. Gao, A. Pogany, and A. W. Stevenson, *Nature* **384**, 335 (1996).
- ¹⁴M. Olbinado, X. Just, J.-L. Gelet, P. Lhuissier, M. Scheel, P. Vagovic, T. Sato, R. Graceffa, J. Schulz, A. Mancuso, J. Morse, and A. Rack, *Opt. Express* **25**, 13857 (2017).
- ¹⁵S. N. Luo, B. J. Jensen, D. E. Hooks, K. Fezzaa, K. J. Ramos, J. D. Yeager, K. Kwiatkowski, and T. Shimada, *Rev. Sci. Instrum.* **83**, 073903 (2012).
- ¹⁶T. Weitkamp, P. Tafforeau, E. Boller, P. Cloetens, J. Valade, P. Bernard, F. Peyrin, W. Ludwig, L. Helfen, and J. Baruchel, *AIP Conf. Proc.* **1221**, 33 (2010).
- ¹⁷A. Rososhek, S. Efimov, S. V. Tewari, D. Yanuka, and Y. E. Krasik, *Phys. Plasmas* **25**, 102709 (2018).
- ¹⁸E. M. Escauriza, M. P. Olbinado, M. E. Rutherford, D. J. Chapman, J. C. Z. Jonsson, A. Rack, and D. E. Eakins, *Appl. Opt.* **57**, 5004 (2018).
- ¹⁹B. L. Henke, E. Gullikson, and J. C. Davis, *At. Data Nucl. Data Tables* **54**, 181 (1993).
- ²⁰D. Yanuka, A. Rososhek, S. Theocharous, S. N. Bland, Ya. E. Krasik, M. P. Olbinado, and A. Rack, *J. Appl. Phys.* **124**, 153301 (2018).
- ²¹See <http://paecinc.us/pt-55.htm> for Pacific Atlantic electronics, model pt-55 series pulser/trigger generator; accessed 14 June 2018.
- ²²M. P. Olbinado, V. Cantelli, O. Mathon, S. Pascarelli, J. Grenzer, A. Pelka, M. Roedel, I. Prencipe, A. L. Garcia, U. Helbig, D. Kraus, U. Schramm, T. Cowan, M. Scheel, P. Pradel, T. D. Resseguier, and A. Rack, *J. Phys. D: Appl. Phys.* **51**, 055601 (2018).
- ²³T. Hiroe, K. Fujiwara, T. Abe, and M. Yoshida, *AIP Conf. Proc.* **706**, 465 (2004).
- ²⁴M. E. Rutherford, D. J. Chapman, T. G. White, M. Drakopoulos, A. Rack, and D. E. Eakins, *J. Synchrotron Radiat.* **23**, 685 (2016).